Annals of Biomedical Engineering, Vol. 46, No. 3, March 2018 *(© 2017)* pp. 498–512
https://doi.org/10.1007/s10439-017-1971-9

Airflow Simulations in Infant, Child, and Adult Pulmonary Conducting Airways

JESSICA M. OAKES,[1] STEVEN C. ROTH,[2] and SHAWN C. SHADDEN[2]

[1]Department of Bioengineering, Northeastern University, Boston, MA, USA; and [2]Department of Mechanical Engineering, University of California, Berkeley, Berkeley, CA 94720, USA

(Received 6 April 2017; accepted 13 December 2017; published online 20 December 2017)

Associate Editor K. A. Athanasiou oversaw the review of this article.

Abstract—The airway structure continuously evolves from birth to adulthood, influencing airflow dynamics and respiratory mechanics. We currently know very little about how airflow patterns change throughout early life and its impact on airway resistance, namely because of experimental limitations. To uncover differences in respiratory dynamics between age groups, we performed subject-specific airflow simulations in an infant, child, and adult conducting airways. Airflow throughout the respiration cycle was calculated by coupling image-based models of the conducting airways to the global respiratory mechanics, where flow was driven by a pressure differential. Trachea diameter was 19, 9, and 4.5 mm for the adult (36 years, female), child (6 years, male), and infant (0.25 years, female), respectively. Mean Reynolds number within the trachea was nearly the same for each subject (1100) and Womersley number was above unity for all three subjects and largest for the adult, highlighting the significance of transient effects. In general, air speeds and airway resistances within the conducting airways were inversely correlated with age; the 3D pressure drop was highest in the infant model. These simulations provide new insight into age-dependent flow dynamics throughout the respiration cycle within subject-specific airways.

Keywords—Computational fluid dynamics (CFD), Multiscale, Lung, Inspiration and expiration.

INTRODUCTION

The structure[18,20,29] and function[16,26] of the pulmonary airways change throughout life, likely influencing ventilation distribution and global and localized respiratory mechanics. While significant efforts have been made in recent years to measure or predict ventilation distribution in healthy human adults,[24,28,40] very little attention has been focused on the juvenile population, despite their heightened sensitively to airborne toxins.[15] Due to practical and ethical considerations, it is mostly unfeasible to study healthy children using advanced imaging or mechanics methodologies beyond what is routinely performed in the clinical setting. However, due to novel advancements in subject-specific computational modeling,[22,31,43] it is possible to perform virtual experiments, enabling insights into age-dependent ventilation differences, which could not be explored previously.

As we age into adulthood, our conducting airways become larger[29] and the number and shape of alveoli in the lung periphery evolve.[3] In addition, tidal and residual volumes, respiration rate,[18] and respiratory compliance increases, while the respiratory resistance decreases during postnatal growth.[26] These morphometric and functional changes likely influences how the air distributes in the lungs, not only effecting flow patterns and breathing mechanics, but distribution of inhaled particulates.[1] Gaining a fuller understanding on how lung physiology and anatomy changes throughout healthy life is paramount to future studies aimed towards using simulation tools to understand and treat pulmonary pathologies, especially those that appear at a young age.

In recent years, there has been a substantial growth in both the number and sophistication of *in silico* respiratory models. Recent simulations have incorporated image-based airway geometry,[27] realistic respiration maneuvers,[30] and lung mechanics.[7,33] By coupling lower dimensional (e.g., 0D or 1D) to image-based 3D lung models,[7,25,35] localized flow patterns can be uncovered while including global respiratory mechanics, a technique that is important when predicting differences between age groups as well as pathological states. As it is not feasible to resolve all geometric

Address correspondence to Jessica M. Oakes, Department of Bioengineering, Northeastern University, Boston, MA, USA. Electronic mail: j.oakes@northeastern.edu

scales of the lung by direct modeling, most work has focused on modeling airflow and particle transport in the extra-thoracic, conducting airways,[4,44] or representative regions of the respiratory zone.[41]

This goal of this current study is to investigate the differences in airflow patterns in subject-specific conducting airways spanning across three different age groups. With this objective, we developed a pipeline that incorporates CT-based airway geometry creation and characterization, calculation of global respiratory parameters, and unsteady airflow simulations. In an attempt to correlate growth to global and local flow distributions, we compare results between subject-specific infant, child, and adult models. By assessing the influence of airway geometry and respiratory mechanics evolution on flow distribution, we aim to understand potential fundamental differences between the age groups.

MATERIALS AND METHODS

Unsteady airflow simulations are performed in an infant, child, and adult pulmonary airway geometries to predict age-dependent variability in airflow and airway resistance. Conducting airway geometric models of an infant, child, and adult subject are constructed from clinically-obtained thoracic CT images and airway dimensions are measured and compared to existing datasets. Physiologically-based simulations are performed by coupling global lung mechanics to the 3D conducting airways where the airflow is driven by the pressure differential between the driving pressure and atmospheric pressure. For each subject, time-dependent flow characteristics are predicted and related to the subject's specific morphometry. The creation of the airway geometries and performance of airflow simulations are described below; further technical details regarding the modeling procedure are described by Oakes *et al.*[32,34]

Geometry Creation and Verification

Spanning from the trachea to the most distal conducting airways distinguishable on the images, 3D conducting airway geometries of an infant, child, and adult (Table 1) are created with the open source software, SimVascular.[43] Image data used to support this study came from thoracic CT images obtained from the SiRFS Stanford Repository. The usage of the CT scans was approved by the Stanford University Institutional Review Board. These CT images were collected from patients with Pulmonary Arterial Hypertension, which is not expected to influence the conducting airway morphology. To verify that the airway geometries were absent from airway abnormalities we consulted with a surgical expert and compared airway morphometric features to data available in the literature. Airway geometries are analyzed with custom built MATLAB codes[34] and airway diameters, path lengths, bifurcation and gravitational angles are compared to reference data.[29,39]

Unsteady Airflow Simulations

Airflow throughout the respiration cycle is calculated by solving the Navier–Stokes equations with physiologically realistic boundary conditions, assuming that the air is incompressible (fluid density: $\rho_f = 1.2E{-}6g/mm^3$), Newtonian (viscosity: $\mu = 1.81E{-}5g/(mms)^1$), and that the walls are rigid:

$$\frac{\partial \mathbf{u}}{\partial t} + [\mathbf{u} \cdot \nabla]\mathbf{u} = -\frac{1}{\rho_f}\nabla p + \frac{\mu}{\rho_f}\nabla^2 \mathbf{u} \tag{1}$$

$$\nabla \cdot \mathbf{u} = 0, \tag{2}$$

where $\mathbf{u}$ and p are the fluid velocity and pressure, respectively. All simulations are performed with the same type of boundary conditions, but individually parameterized. Airflow is driven by a pressure differential between the terminal airways ($\Gamma_{i,j}$ where i and j are the airway and lobe numbers, Fig. 1) and the trachea ($\Gamma_{trachea}$). Assuming negligible pressure drop between the mouth and trachea, we set the trachea pressure equal to atmospheric ($P_{atm} = 0$ cm H_2O gage). At the airway walls (Γ_{wall}, Fig. 1) a no slip boundary condition is prescribed.

Boundary condition descriptions at the distal faces ($\Gamma_{i,j}$) are not straightforward, as neither the time-dependent flow or pressure can be experimentally measured directly. Thus, it is necessary to choose these boundary conditions carefully, in order to best represent physiological conditions. In the respiratory system, flow in and out of the lungs is driven by the diaphragm motion, which in turn creates a negative pressure within the pleural cavity. This pressure must overcome the pressure gradients caused by the respiratory compliance and resistance to draw air in and out of the lung. To mimic this process with our simulations, we choose to prescribe resistance and compliance networks, driven by the time-dependent driving pressure, $P_D(t)$, to each of the distal faces, $\Gamma_{i,j}$. The respiratory resistance and compliance values, as well as the definition of the driving pressure are described below.

Global Respiratory Parameters

Global respiratory parameters, including tidal volume (TV), respiratory rate (RR), mean flow rate

TABLE 1. Subject data.

	Age (years)	Weight (kg)	Height (cm)	Gender
Infant	0.25	6.1	55.2	Female
Child	6	18.8	115	Male
Adult	36	59.8	160	Female

(Q_{mean}), resistance (R_{global}) and compliance (C_{global}), were calculated for each subject based on their age, gender, weight, and height. Measuring global respiratory mechanics in 63 children spanning ages 3 weeks to 15 years, Lanteri and Sly[26] report empirical relationships as a function of gender and height; we employ these relationships to estimate dynamic respiratory resistance and compliance for the infant and child models. In 16 adult patients with no history of cardiopulmonary disease, D'Angelo *et al.*[9] measured dynamic compliance and resistances in sedated patients; average values were employed here for the adult subject. Analyzing data collected from multiple sources, Hoffman[18] reported age-dependent relationships for TV and RR, and these were applied here for the infant and child subjects. For the adult subject, commonly accepted TV and RR values are employed, which fall within ranges reported by several sources.[2,18]

Driving Pressure Calculation

Experimental measurement of pleural pressure, $P_P(t)$, is not straightforward and not performed during routine visits to the clinic. Alternatively, pleural pressure may be calculated if the pulmonary resistance and compliance are known. In this current study, we are modeling tidal breathing, driven by a pressure that must overcome the respiratory resistance and compliance to drive air into and out of the airways. Thus, we set this driving pressure $P_{\mathrm{D}}(t) = P_{\mathrm{P}}(t) + \frac{\mathrm{FRC}}{C_{\mathrm{global}}}$, taking into account the initial lung volume at rest (FRC). Assuming the respiration waveform, R_{global}, and C_{global} are known, the driving pressure can be set as

$$P_D(t) = R_{global}Q(t) + \frac{V(t)}{C_{global}} - P_{atm} \tag{3}$$

where $Q(t) = \frac{dV(t)}{dt}$. Assuming a sinusoidal respiration waveform, we define the time-dependent breathing volume, $V(t)$ as:

$$V(t) = -\frac{1}{2}\left[TV\cos\left(\frac{2\pi}{T_B}t\right) + TV\right], \tag{4}$$

where T_B is the total time for one breath, defined as $\frac{1}{RR}$. Note, the sign convection indicates flow direction; negative and positive flow rate for inhalation and exhalation, respectively. Employing each subject's respiratory parameters (Table 2), $P_D(t)$ is calculated for each subject.

Prescribing Respiratory Mechanics at $\Gamma_{i,j}$

To model airflow within the 3D airways, appropriate and physiologically-realistic boundary conditions must be implemented. To do this, we sectioned the lung into the directly modeled 3D region, and the indirectly modeled lumped-parameter (0D) region. These regions were then linked together with boundary condition descriptions. Airflow in and out of the lungs is driven by the difference between the driving pressure, $P_D(t)$, and the atmospheric pressure (P_{atm} is set to 0 cm H_2O at the trachea, Fig. 1). As this total pressure drop includes both the 3D and 0D domains, $P_D(t)$ must overcome both P_{0D} and P_{3D} to move flow in and out of the lungs. The 3D pressure drop, P_{3D}, is a result of the airflow resistance, calculated from the 3D simulation, and is a function of the fluid properties, airway geometry, and airflow characteristics. P_{0D} represents the pressure drop distal from the 3D geometry, incorporating viscous airflow resistance and the resistance and compliance of the pulmonary tissue and thoracic cavity. Distal pressure drop may be described by simple lumped-parameter resistance-compliance networks. Namely, at each step of our Navier–Stokes solver, we solve

$$P_{\Gamma_{i,j}} = R^n_{i,j}\frac{dV_{\Gamma_{i,j}}}{dt} + \frac{V_{\Gamma_{i,j}}}{C_{i,j}} + P_D, \tag{5}$$

by passing flow rate to $\Gamma_{i,j}$.[13] Here, $V_{\Gamma_{i,j}} = \int_0^t \int_{\Gamma_{i,j}} \mathbf{u}\cdot\mathbf{n}\,\mathbf{ds}\,\mathbf{dt}'$; $\mathbf{u}$ is the air velocity, calculated by solving the Navier–Stokes equations (Eqs. (1) and (2)), and $\mathbf{n}$ is the unit vector normal to the boundary. Note, that Eq. (5) represent the pressure drop distal to the 3D geometry and therefore does not account for the 3D pressure drop P_{3D}. As we assume that our 3D airways are rigid, compliance is not affected by the 3D geometry and therefore, assuming that the delivered air volume is proportional to the subtending lobe volume and cross-sectional area of the distal airway ($A_{i,j}$); we set $C_{i,j} = \frac{A_{i,j}\alpha_j C_{global}}{A_{T_j}}$, where α_j is the lobe volume fraction (0.25, 0.20, 0.25, 0.09, 0.21, for the left inferior and superior, and right inferior, middle, and superior lobes,

respectively)[19] and $A_{T_j} = \sum_{i=1}^{N_{airway}} A_{i,j}$ is the total cross-sectional area of all the airways within each lobe j.[32] The 3D resistance is not negligible and cannot be predicted a priori due to the complex geometry and flow structures. Initially, we set $R_{i,j}^n = \frac{A_{T_j} R_{global}}{A_{i,j}\alpha_j}$. Following each unsteady simulation, we update $R_{i,j}^n$, accounting for the 3D resistance by solving $R_{i,j}^n = \frac{dt}{dV_{\Gamma_{i,j}}}\left[\Delta P_{\Gamma_{i,j}} - V_{\Gamma_{i,j}}\right]$, where $\Delta P_{\Gamma_{i,j}}$ is pressure drop from the trachea to each distal face and is calculated from the simulation results, and $\frac{dV_{\Gamma_{i,j}}}{dt}$ and $V_{\Gamma_{i,j}}$ are the expected flow rate and volume, respectively. We iterate unit $R_{i,j}^n$ is within 5% of $R_{i,j}^{n-1}$, where n and $n-1$ represents the current and previous simulation, respectively.

Numerical Calculation of Airflow

The incompressible Navier–Stokes equations (Eqs. (1) and (2)) are solved with the flow solver available in Simvascular, an open-source software package developed for physiological flow simulations.[43] A stabilized Galerkin finite element method with a custom linear solver that incorporates a combination of GMRES and conjugate gradient methods is employed.[12] The second order generalized α-method is used for the time integration. To avoid numerical instability at $\Gamma_{trachea}$ and $\Gamma_{i,j}$ we apply a backflow stabilization framework,[13] with $\beta = 0.1$. Tetrahedral elements with boundary layer refinement are created with Meshsim (Simmetrix Inc., Clifton Park, NY). Rigorous mesh-sensitivity studies are performed to ensure that the results were independent of the mesh resolution. Test mesh sizes ranged between 0.3 to 15 million elements with varying amounts of boundary layer refinement. A final mesh size of 11, 5, and 5 million elements are used for the adult, child, and infant models, respectively. These mesh sizes ensured that mass is conserved within 0.01%. A time step of 1E−4 s is employed, with up to 7 non-linear iterations per time-step.

RESULTS

Airway Geometries

The 3D airways span up to 11, 9, and 9 generations for the adult (Fig. 1a), child (Fig. 1b), and infant (Fig. 1c), respectively. Due to image resolution limitations and the smaller dimensions of the juvenile lungs, the image-based 3D airways for the infant and child had 23 and 37 terminal airways, compared to 40 terminal airways in the adult geometry. The surface area of the 3D airway walls are 20.6, 60.5, and 172 cm^2 for the infant, child, and adult, respectively. To highlight the differences between the three geometries, video files of the rotating airways are provided within the supplementary materials. The infant model is considerably more planar than the adult and child models. In addition, the main branch leading to the left inferior lobe is relatively smaller in the infant model compared to the other two models.

Airway diameters and lengths for the three geometries are presented in Fig. 2. Dimensions were measured directly from the geometric models created from the CT images and are presented as the mean and standard deviation per generation. As the beginning of the trachea is not distinguishable on the CT images, it is not possible to measure the trachea length. Similarly, the terminal airway lengths are not reported. We compare dimensions to those previously reported for subjects with similar age and height,[29,38] Employing measurements collected from airway casts of subjects spanning ages 11 days to 21 years old, Phalen and Oldham[38] correlated airway lengths and diameters to the subject's height, incorporating generation-dependent coefficients. Similarly, Ménache *et al.*[29] report morphometric data for subjects ages 0.25 to 21 years old, correlated to age-dependent coefficients and generation numbers. Note, that while Ménache *et al.* report dimensions of an infant the same age as the one analyzed here (0.25 years), their dataset did not include a 6 year old child. Therefore, we used the closest aged subject (8.67 years). Shown in Fig. 2, the airway dimensions typically lay in-between the previously reported correlations. The largest differences can be seen for the first couple of airway generations, where our measurements are smaller than reported by Phalen and Oldham[38] and larger than reported by Ménache *et al.*[29] for the infant and child models. In contrast, the trachea diameter of the adult is slightly larger than values previously reported (Fig. 2a). In addition, as only the larger airways within a given generation are distinguishable on the CT images, later generation airway diameters are larger than relationships that include all (i.e., small) airways (Fig. 2).

Estimated Respiratory Parameters

Global flow characteristics and mechanics estimated from the empirical relations are given in Table 2. As expected, lung volumes (TV and FRC) increase with age. In addition, the ratio of TV to FRC is larger in the infant ($\frac{TV_I}{FRC_I} = 0.54$) and child ($\frac{TV_C}{FRC_C} = 0.25$) than in the adult ($\frac{TV_A}{FRC_A} = 0.17$). This indicates that, with respect to the resting lung volume (FRC), the amount of inhaled air (TV) is

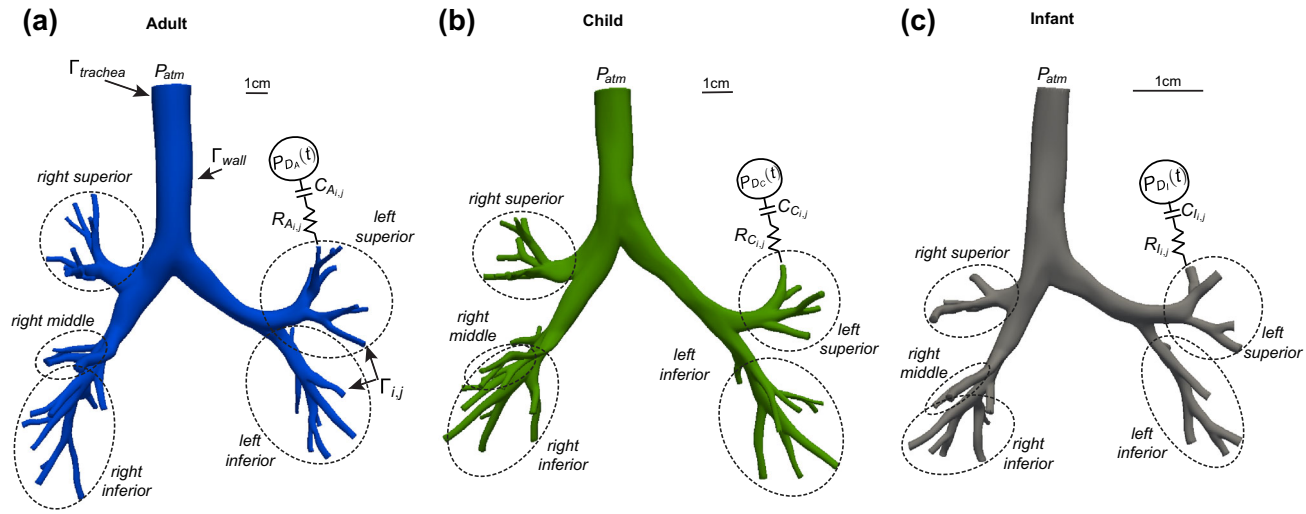

FIGURE 1. Three-dimensional image-based airway geometries of an adult (panel a), child (panel b), and infant (panel c). Airways leading to each lobe are outlined as well as the airflow boundary conditions. Scale bars (1 cm) are shown for the three models.

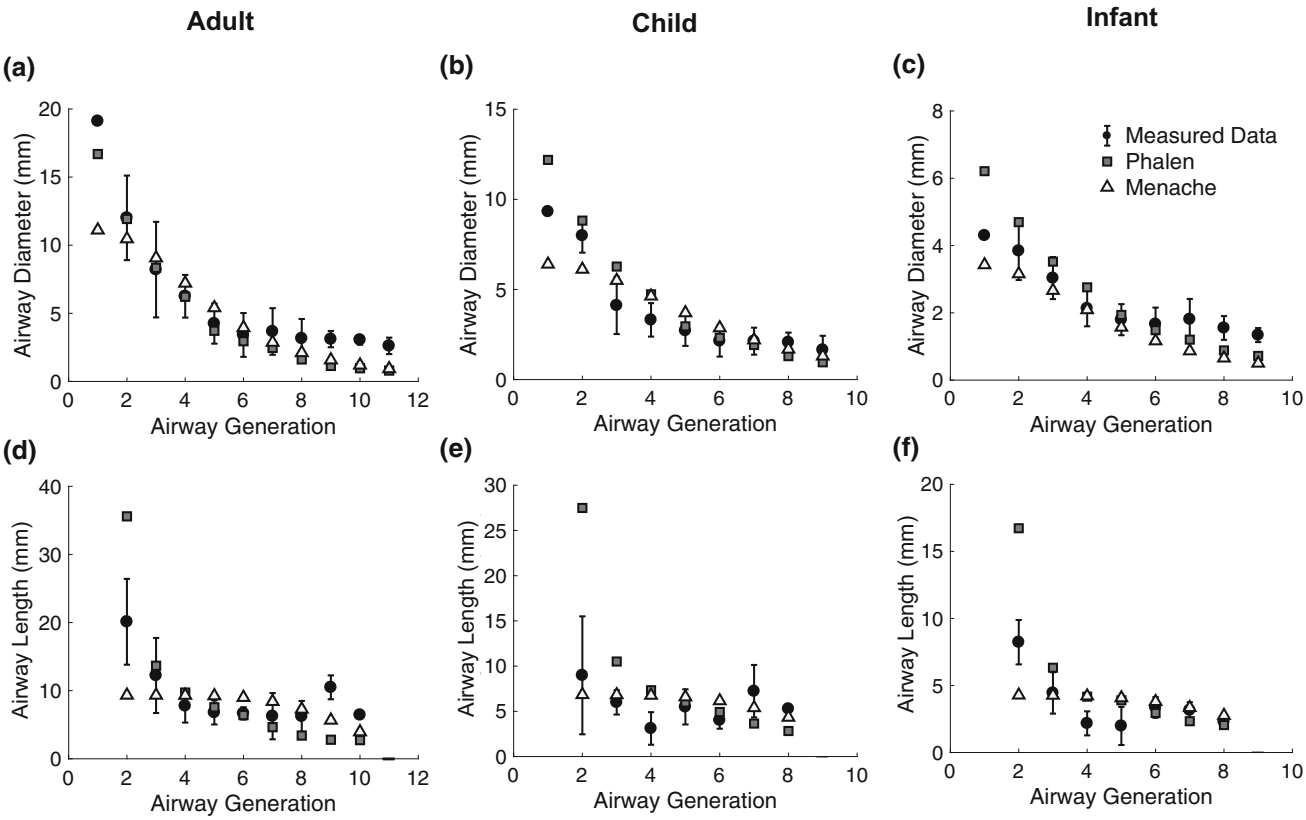

FIGURE 2. Airway diameters (panel a: adult, panel b: child, panel c: infant) and lengths (panel d: adult, panel e: child, panel f: infant) for each generation. Measured data is compared to morphometric information provided by Phalen and Oldham[38] and Ménache *et al.*[29] Error bars represent the measurement standard deviation between all airways within a given generation. Note, trachea airway length (generation 1) is not reported, as the start of the trachea is not visible on the CT images.

greater in youth than in adults. While RR decreases with age, Q_{mean} increases, as the decrease in RR from infant to child is two-fold, while TV is four times higher in the child compared to the infant (note: $Q_{mean} = TV \times RR$). Calculated from the empirical relationships, respiratory resistances decreased and compliances increased with age (Table 2).

Global Airflow Characteristics

Non-dimensional parameters, Reynolds ($Re = \frac{4\rho Q}{\pi\mu D_{trachea}}$, where Q is either Q_{mean}: mean flow rate during inspiration or Q_{max}: maximum flow rate) and Womersley numbers ($Wo = D_{trachea}\sqrt{\frac{2\pi\rho}{RR\,\mu}}$) are presented in Table 3. *Re*, the ratio of inertial to viscous forces, was similar between models and less than the expected criteria necessary for turbulent flows in conduits. Note, *Wo*, represents the importance of transient inertial forces with respect to the viscous forces; larger values of *Wo* indicate a stronger time-dependence. Womersley numbers are larger than unity for all three models and increased with age, signifying the importance of the transient flow field.

The maximum driving pressure, $P_D(t)$ increases with age; $P_{D_A}(t)$ is much smaller than $P_{D_C}(t)$ and $P_{D_I}(t)$ (Figs. 3a and 3d). Plotted as the summation of the flow rates at each of the terminal airways within each lobe, the proportion of air volume entering each lobe is the same between the three models (Figs. 3d and 3f), as the same lobe fraction was employed to calculate $R_{i,j}$ and $C_{i,j}$. Pressure is negative at the terminal airways during inspiration and positive during expiration (Figs. 3g and 3i), relative to the pressure set at the trachea ($P_{trachea}$ =0). During expiration, the left superior pressure is larger throughout time for all three models. In contrast, the left inferior lobe exhibited the largest pressure during inspiration in the child model (Fig. 3h) and the left inferior and superior lobes had nearly the same pressure during inspiration in the adult model (Fig. 3g).

Airflow and Pressure Characteristics in the 3D Geometries

Pressure at time of maximum inhalation and exhalation are shown in Fig. 4 for the three models. The 3D pressure drops are less than 10% of the respiratory driving pressures (Fig. 4). During inhalation, the flow stagnates at the main bifurcation, causing localized regions of increased pressure, Fig. 4. Non-uniform distribution of pressure is seen at the main carina because the air rapidly changes direction to fill in the left and right lungs (Fig. 5). The pressure drop from the trachea to the distal airways is largest in the infant model for both inhalation (Fig. 4c) and exhalation (Fig. 4f). Locations of large pressure differentials are the same between the three models, located at the area of the reduced cross-section of the left main bronchi. Plotted as the average pressure over all the terminal airways within each lobe, the larger pressure drops in the infant model are also highlighted in Fig. 3(i). In contrast to the adult and child models, the left superior lobe exhibited the largest pressure drop for inspiration and expiration (Fig. 3i). While the largest pressure drop are seen in the left superior lobe for exhalation, the left inferior lobe exhibited the largest pressure drop during inhalation in the adult (Fig. 3g) and child (Fig. 3h) models. Highlighted in the 3D geometries (Fig. 4), the pressure more rapidly changed along the main left bronchi for all three models.

Velocity magnitudes at peak inhalation (panels a–c) and exhalation (panels d–f) are shown for the three models in Fig. 5. In addition, velocity magnitudes at various locations along the main bronchi are shown in Figs. 6, 7 and 8 for the adult, child, and infant, respectively; the velocity magnitudes are shown with colored contour plots with secondary flow streamlines and velocity vectors overlaid. Peak velocity magnitudes are inversely correlated to age: the airflow is faster in the infant model compared to the other two. For all three models, peak velocity is found at the left main bronchi just upstream of the bifurcation that leads to the superior and inferior left lobes where the cross-sectional areas are reduced (Fig. 5). During inspiration, the velocity profile in the trachea of the healthy adult (Fig. 6, location 1) is more plug-like than the child (Fig. 7) and infant (Fig. 8), where the velocity profile is more parabolic. This occurs because *Wo* is larger in the adult (Table 3).

Inhaled air starts at the trachea entrance and passes through each of the bifurcations and exits out of the distal airways. Airflow speed is highest closest to the inside of the bifurcation. Depending on the combined influence of the airway's girth and curvature, the resulting adverse pressure gradient (Fig. 4) will cause flow to separate. For example, Figs. 5a–5c illustrates areas of flow separation and recirculation distal to some of the bifurcations during inhalation. In Fig. 9 we highlight the 3D nature of the flow field by plotting streamlines at peak inspiration and expiration. Loosely

TABLE 2. Respiratory parameters employed in CFD simulations.

	TV (mL)	*FRC* (mL)	*RR* (breaths/s)	Q_{mean} (mL/s)	R_{global} (cm $H_2$0-s-mL^{-1})	C_{global} (mL-cm H_2 0^{-1})
Infant	49	81	0.66	65	8.02E−2	5.19
Child	209	830	0.32	135	2.44E−2	23.1
Adult	500	3000	0.25	250	7.0 E−3	59

TABLE 3. Dimensionless flow parameters (Reynolds numbers; $Re_{mean} = \frac{4\rho Q_{mean}}{\pi\mu D_{trachea}}$ and $Re_{max} = \frac{4\rho Q_{max}}{\pi\mu D_{trachea}}$, Womersley number; $Wo = D_{trachea}\sqrt{\frac{2\pi\rho}{RR\mu}}$, where f is the respiration frequency) and the average ($R_{3D_{mean}} = \frac{\Delta P_{mean}}{Q_{mean}}$) and maximum ($R_{3D_{max}} = \frac{\Delta P_{max}}{Q_{max}}$) 3D flow resistance for each subject.

	Re_{mean}	Re_{max}	Wo	$R_{3D_{mean}}$ (cm H_2O s/mL)	$R_{3D_{max}}$ (cm H_2O s/mL)
Infant	1147	1746	2.52	4.8E−3	2.9E−1
Child	1166	2006	3.59	2.1E−3	3.3E−1
Adult	1072	1740	6.13	3.42E−4	4.8E−2

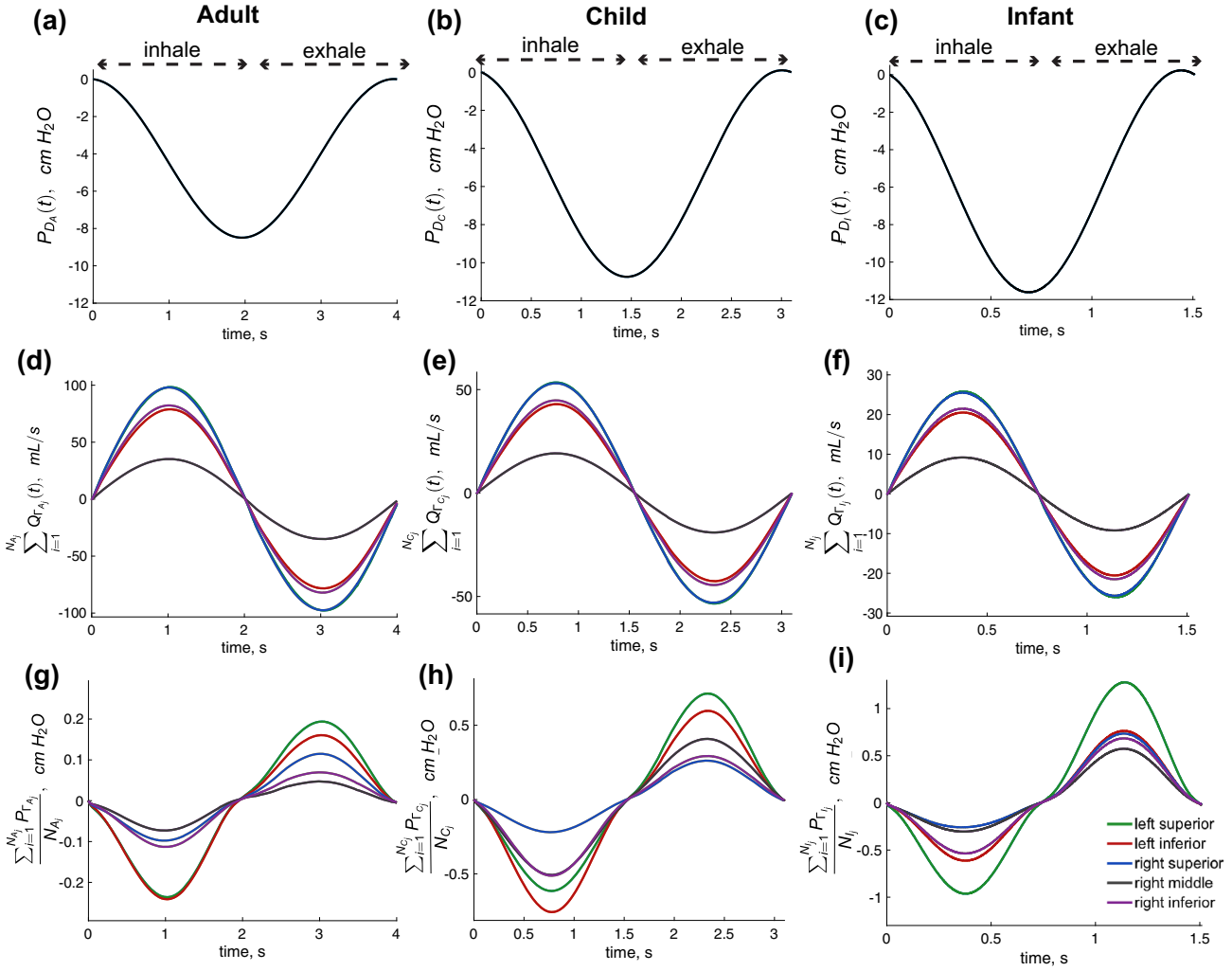

FIGURE 3. Driving pressure, $P_D(t)$ employed for the adult (a), child (b), and infant (c) simulations. Panels (d–f) show the flow rate, summed over all the airways within each lobe, for the adult, child, and infant models, respectively. The average pressure of the terminal airways within each lobe are shown for the adult (panel g), child (panel h), and infant (panel i) models.

correlated to the magnitude of the bifurcation angles, helical flow structures are observed within the left superior lobe of the adult (Fig. 9a) and infant (Fig. 9e) during inspiration. Deans number ($De = \sqrt{\frac{d}{2r}}Re$, where r is the radius of curvature (calculated from three points along the airway's centerline) and d is the conduit diameter) characterizes flow in curved vessels based on the ratio of combined inertial and centripetal forces with respect to the viscous forces. Deans numbers are shown for each cross-section (Figs. 6, 7, and 8). Compared to the other two models, De is smallest at position 5 child model, because of the small radius of curvature, resulting in less secondary flow motion. Secondary flow motions are largest in the infant (Fig. 8) than the child (Fig. 7) and adult (Fig. 6). As evident by the streamline density, cross-sections with the largest De correlate with the largest secondary

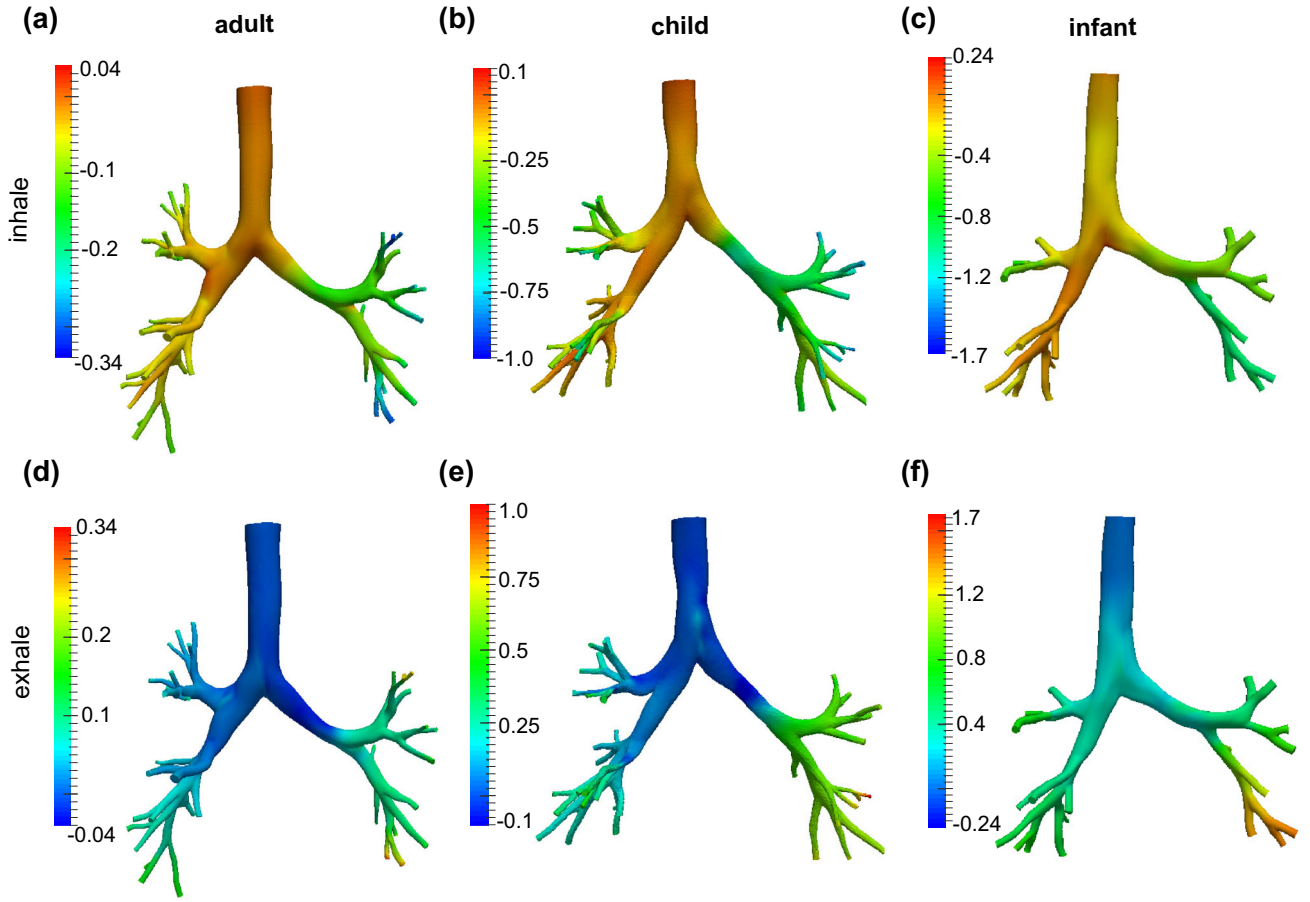

FIGURE 4. Color maps of the pressure (cm H_2O) on the surface of each of the three models at times of maximum inhalation (panels a–c) and exhalation (panels d–f). Note that the positive and negative pressure values during inhalation and exhalation, respectively, are located at the main carinas. Pressure is set to zero at $\Gamma_{trachea}$.

motion for inhalation in the infant airways (Fig. 8). Differences in the flow structures between the three geometries is likely a combination of *De*, *Wo*, and *Re* (Table 3), as well as variations in the airway shapes, including airway cross-sectional ellipticity. For each geometry, flow structures that form just distal to the bifurcation during inspiration propagate into the daughter branch. While the secondary flow structures tend to dissipate within a few diameters, the flow generally does not have sufficient time/length to become fully developed.

During exhalation air travels from the distal branches up towards the trachea. In general, airflow is more complex during exhalation, as air originating from daughter bronchi merge together within their parent branch (Figs. 5d and 5f compared to a and c). As highlighted in Fig. 9, air originating from the various five lobes form helical structures within the trachea. Similar flow structures are also observed within the main left bronchi of the infant (Fig. 9f), likely due to the high speed flow coming from the inferior left lobe. These structures are linked to air speed differences within the two daughter branches. For example, as shown in the trachea cutouts (location 1) in Figs. 6, 7, and 8, secondary flow structures within the trachea are caused by high speed regions originating from the left main bronchi (position 5). Peak speed locations depend on bifurcation symmetry; for example both the adult and child main carina bifurcation angles are similar, resulting in peak speeds located in the center of the trachea (position 1, Figs. 7 and 6). In contrast, the bifurcation angle of the left main bronchi is larger than the right main brochi in the infant (Fig. 8), resulting in skewed peak speeds within the trachea. For the infant, peak speeds are found in the airway leading to the left inferior lobe (position 6, Fig. 8) for both inspiration and expiration. This is likely because the cross-sectional area at this position is smaller (3.6 mm^2) than the airway leading to the left superior lobe (6.8 mm^2), despite the left inferior lobe having a higher flow delivery fraction (0.25) than the superior lobe (0.2). Recirculation is present at peak expiration at the outer

left bronchi of the adult (Fig. 5d) and at the infant and child's main carinas (Figs. 5e and 5f).

Airway resistances are inversely correlated with age, as shown by the global (Table 3) and generation-based (Fig. 10) 3D airflow resistances. Calculated by dividing the pressure drop across each airway by its mean flow rate, airway resistances were larger during expiration than inspiration for the infant and child models. In contrast, not only is $R_{3D_{mean}}$ an order of magnitude smaller in the adult compared to the juveniles, but there are minimal differences between inspiration and expiration. None of the measured resistances matched well with values calculated using the Poiseuille flow profile assumptions ($R_{Poise} = \frac{64\mu l}{\pi d^4}$, where l and d are the length and diameter of the airway, respectively), Fig. 10. To further highlight the variability in the 3D airway resistances, we calculate $R_{3D_{max}}$ for the airway with the largest 3D resistance (Table 3); the largest 3D values are located in the left inferior lobe for all three models.

DISCUSSION

To date, little attention has been focused on predicting airflow distributions and airway mechanics in child lungs. This is mainly because it is infeasible to perform extensive experiments in children. On the other hand, *in silico* simulations may provide insight into airflow characteristics, including airway resistances, within the conducting airways. To address the need of understanding fundamental respiratory flow

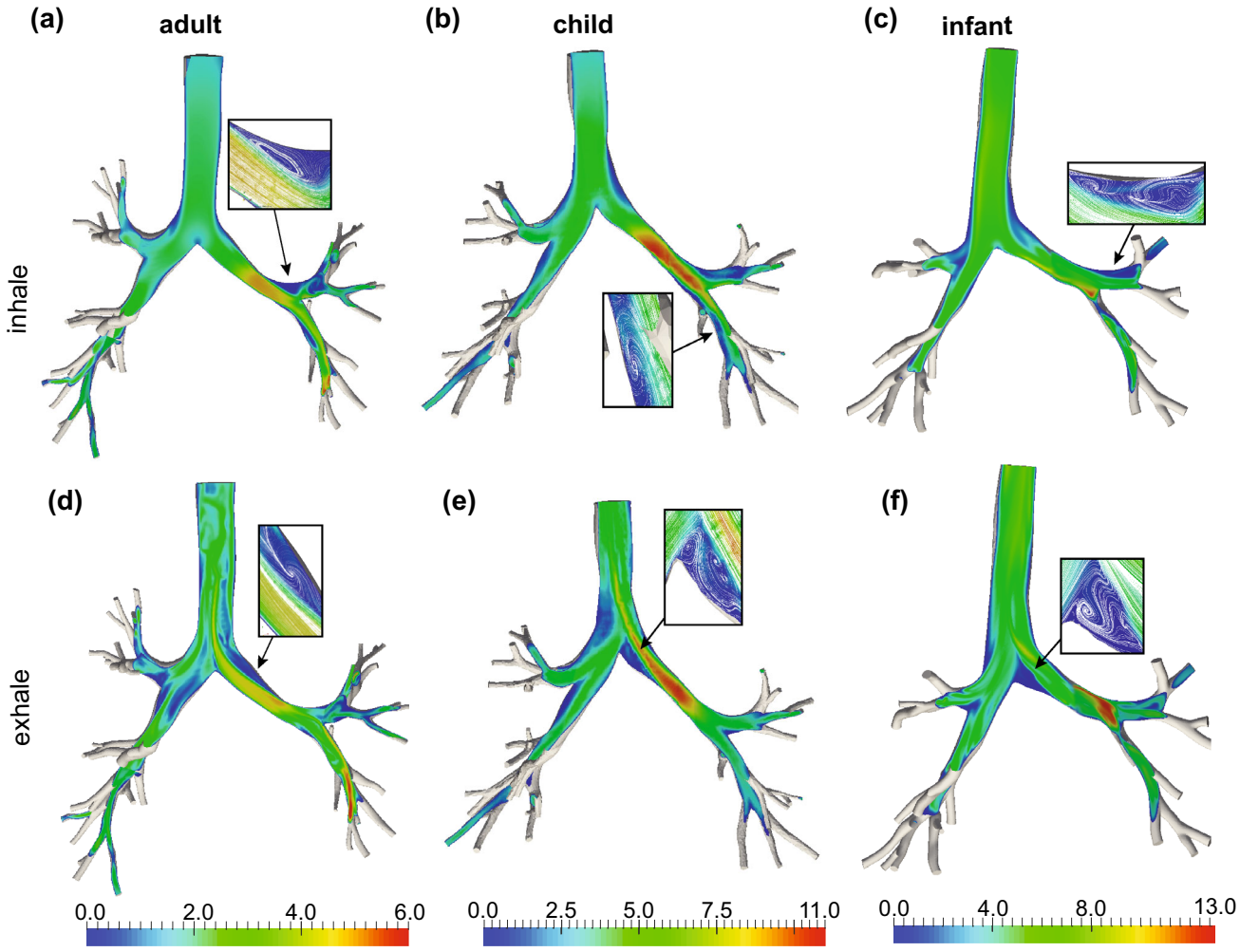

FIGURE 5. Velocity magnitudes (m/s) through the center of the adult (panels a and d), child (panels b and e) and infant (panels c and f) at maximum inhalation (panels a–c) and exhalation (panels d–f). Note that the same velocity range was used for both inhalation and exhalation for each of the models. Regions of flow separation and recirculation are highlighted within each panel (not shown to scale).

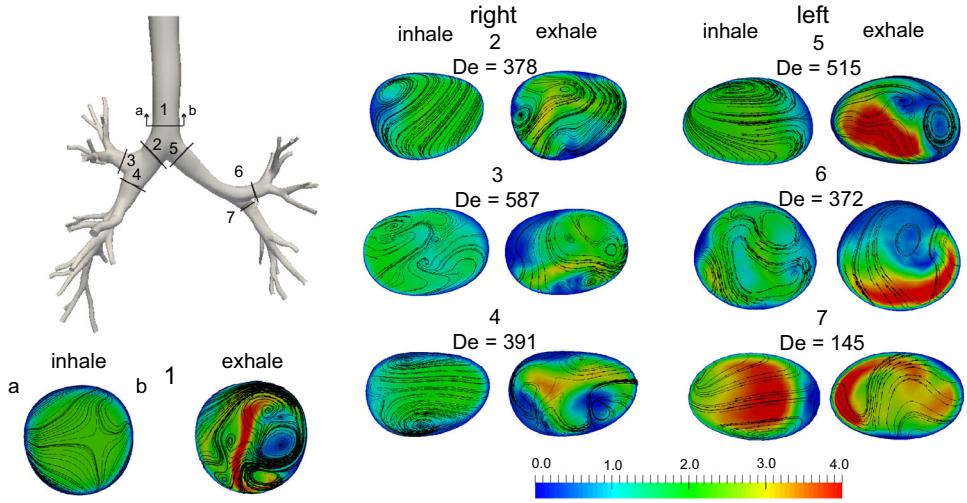

FIGURE 6. Cross-sectional plots of velocity magnitude (m/s, accounting for all three components of velocity) for various locations along the main bronchi at peak inhalation and exhalation. All color plots are shown along the same scale. For each cross-section, secondary streamlines and velocity vectors are overlaid on top. Note, the size of each cut-out is not to scale.

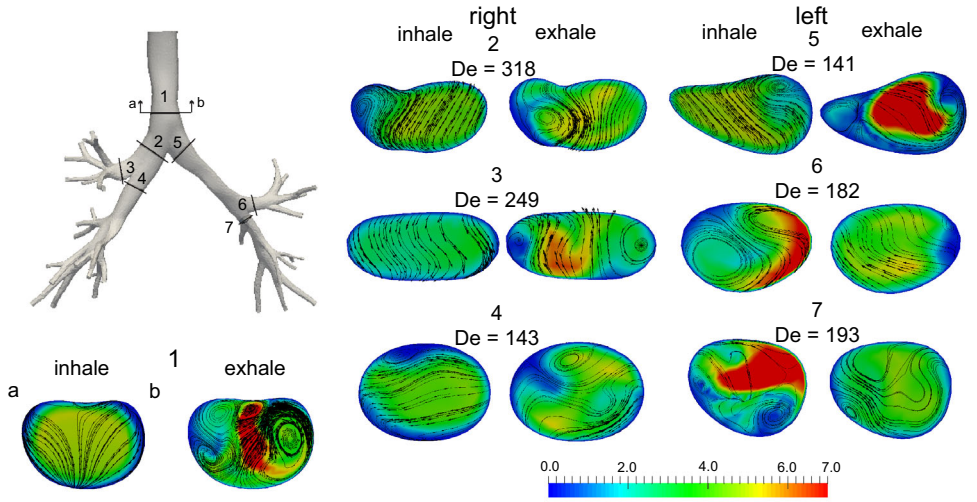

FIGURE 7. Velocity magnitude (m/s) and secondary streamlines and velocity vector plots for the child airways. Plots are shown for peak inhalation and exhalation and various locations throughout the main branches. Note, the size of each cut-out is not to scale.

differences between children and adults, we simulated airflow throughout the respiration cycle in patient-specific infant, child, and adult airway models by coupling image-based geometries to global respiratory mechanics. These simulations provide a first glimpse into airflow differences between age groups.

One of the main challenges in simulating airflow in the lung is prescribing realistic boundary conditions. This is because it is currently impossible to experimentally measure time-dependent flow rates or pressures at the terminal airways. One way to overcome this limitation is to incorporate distal respiratory mechanics into the computational framework. By doing this, whole-respiratory system dynamics may be coupled with localized flow simulations in specific areas of interest (e.g., conducting airways). This technique has been widely employed to study flows in the cardiovascular system,[14] and more recently, in the respiratory system of rodents[33] and adult humans.[7,25] While assumptions regarding partitioning of the distal respiratory mechanics is necessary with this approach, parameterization is individualized based on the patient image data. Alternative methods, such as prescribing volumetric flow rates modeled from lung deformation measured with CT[10,30] may be employed, if multiple CT images are acquired throughout the breathing cycle, which was not the case here. Either technique, lung deformation or distal mechanics (as employed here),

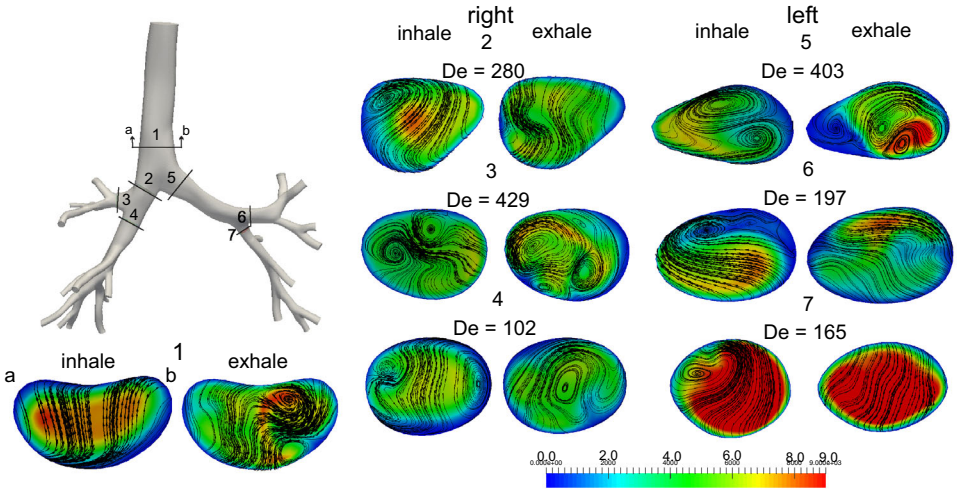

FIGURE 8. Similar to Figs. 6 and 7, velocity magnitudes (m/s) and secondary streamlines and velocity vectors are shown for the infant airway model at peak inhalation and exhalation. Peak velocity magnitudes are seen for slice 7, likely because of the relatively smaller airway caliper feeding the inferior left lobe. Note, the size of each cut-out is not to scale.

are expected to be more realistic than prescribing uniform or zero pressure,[23] a traction-free condition, or uniformly distributed volumetric flow rates[5,42] at the distal airways. Airflow distributions with traction-free or uniform pressure boundary conditions are determined solely based on the 3D conducting airway geometry; whereas in reality, flow is driven mainly by the distal mechanics, which is consistent with the approach used herein. Note, with our 3D–0D coupling method, we do not need to prescribe a velocity profile at the outlets, enabling velocity profiles to be calculated as part of the solution. Prescribing flow rate requires a velocity profile (e.g., parabolic) to be described within the boundary condition definition. It should be noted with our choice of boundary condition, it was necessary to define a respiration flow rate. We choose a sinusoidal function (Eq. (4)) as it is a suitable assumption for breathing at rest.

As the lung ages from infancy to adulthood, the airway dimensions increase (Fig. 1) and the elastic recoil pressure decreases as the airways are pulled open,[26] resulting in a reduction of total respiratory resistance. Airway resistance, if Poiseuille flow is assumed, is inversely correlated to the fourth power of airway diameter ($R_{Poise} = \frac{64\mu l}{\pi d^4}$, where l and d are the length and diameter of the airway, respectively). While airway resistance cannot be calculated with this simple relationship, because the flow patterns are complex (Figs. 6, 7, 8, and 10), we may expect that the trend (higher resistances with smaller airways) is true. Furthermore, the mean airway resistance (4.7E−3 $\frac{\text{cm}\,H_2O\,\text{s}}{\text{mL}}$) in the infant is similar to airway resistance (R_{raw}) to values found by Hall *et al.*[17] in a baby of similar height (2.05E−3 $\frac{\text{cm}\,H_2O\,\text{s}}{\text{mL}}$). R_{raw} reported by Lanteri and Sly falls within the range found here (Table 3) for both the infant (3.5E−2 $\frac{\text{cm}\,H_2O\,\text{s}}{\text{mL}}$) and child (1.35E−2 $\frac{\text{cm}\,H_2O\,\text{s}}{\text{mL}}$)[26] airways. Similar conclusions can be made for the adult airways; the mean R_{raw} reported by DuBois *et al.*[11] (1.50E−3 $\frac{\text{cm}\,H_2O\,\text{s}}{\text{mL}}$) lies in-between our mean and maximum calculations. Note, our airway resistance calculations does not encompass the entire lung, therefore we would expect our airway resistances to double[36] (mainly because resistances within each generation are added in parallel, $\frac{1}{R_{total}} = \sum_{i=1}^{N} \frac{1}{R_i}$). Note, the 0D models account for the remaining airway resistances and the tissue/chest wall resistances. Respiratory resistance and compliance are a combination of lung and thoracic cavity mechanics, including the chest wall. Lung resistance is a combination of the pressure drop due to the airflow and energy losses associated with the deformation of the parenchyma.[21] In addition, our simulation results agree with predictions made by Xi *et al.*[44] in the extra-thoracic airways of an infant, child, and adult.

While flow speeds are higher in the infant model compared to the other two (mean speed in the trachea for the infant, child, and adult are 313, 212, and 88.2 cm/s, respectively) Reynolds numbers are nearly the same for all three models (Table 3). On the other hand, Womersley number increase with age (Table 3) and are above unity for all three subjects. In general, similarities in the flow structures exists between the models. For example, all three models have peak flow regions in the main left bronchi throughout inspiration

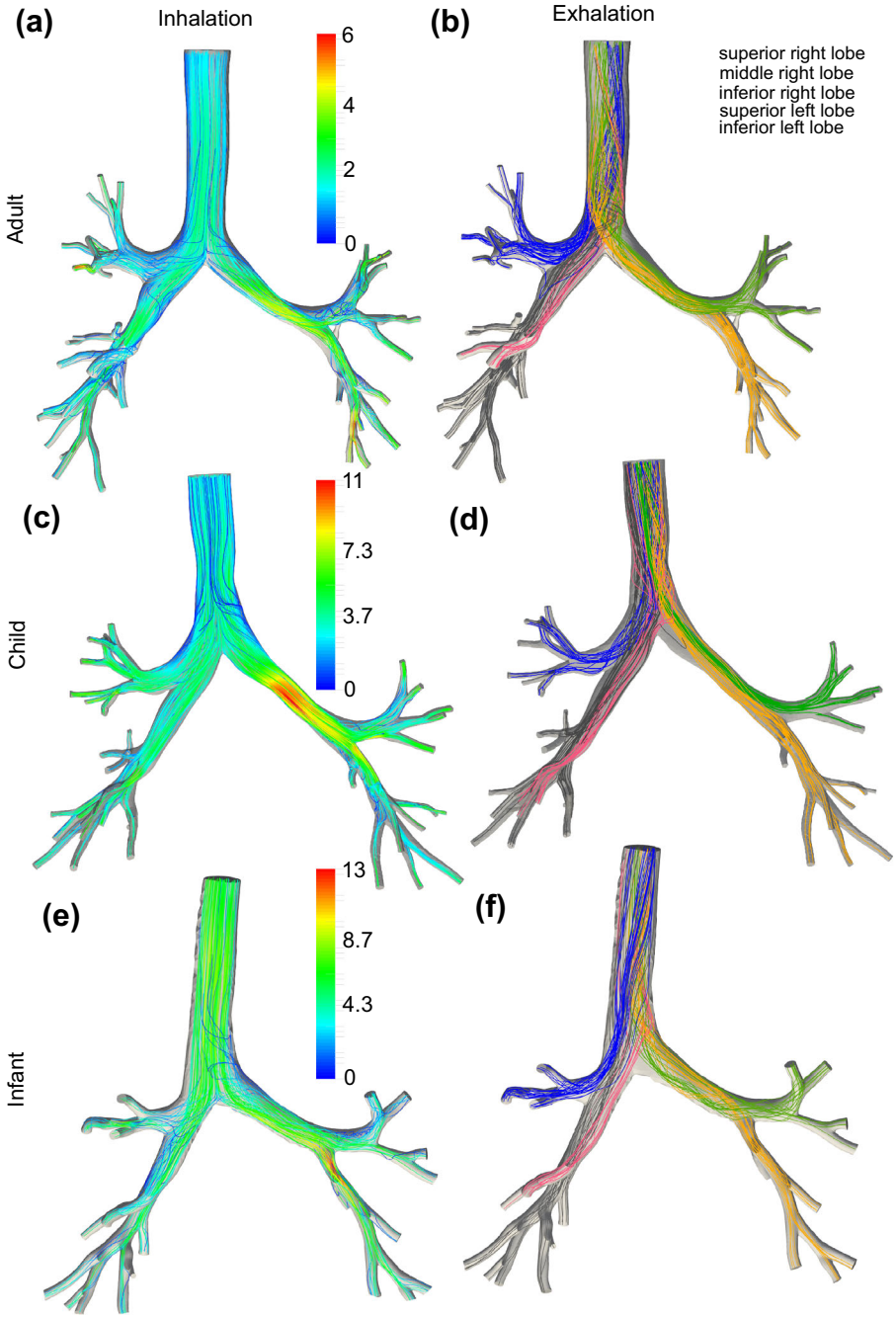

FIGURE 9. Streamlines at peak inspiration (velocity magnitudes, m/s: panels a, c and e) and expiration (panels b, d, and f). Colors for exhalation are generated based on the lobe that the flow originates from.

and expiration and these areas of high flow velocity continue well into the trachea during exhalation (Fig. 5). Within some bifurcations, helical structures form during inspiration, specifically downstream of the bifurcations leading to the superior left and middle right lobes of the adult. The airflow is more distributed during exhalation, likely because of the flow phenomenon caused by two high speed jets merging together within a single airway. Downstream, the strong jets begin to break, as highlighted within the trachea of the adult, Fig. 5d. In addition, the child and infant both have pockets of low speed near the main carina during exhalation, whereas low speed and recirculating flow areas are found in the right main bronchi of the adult. Secondary flow motions (Figs. 6, 7, and 8) are important as they contribute to the airflow resistance. In addition, secondary motion may guide particles towards the airway walls, enhancing particle deposi-

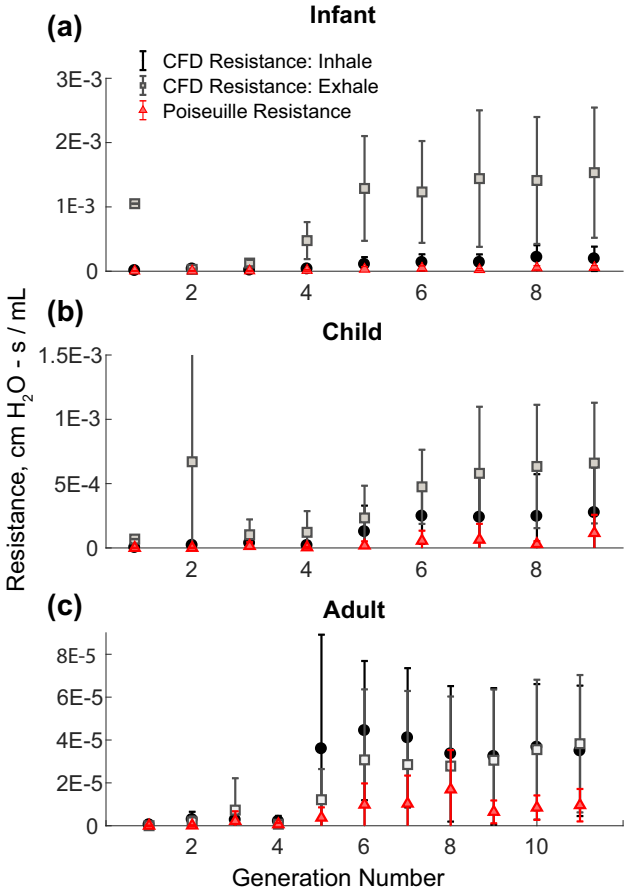

FIGURE 10. Generation-based airway resistances for the infant (panel a), child (panel b), and adult (panel c) at peak inspiration and expiration. Values are calculated for each airway by dividing the pressure drop by the mean flow rate, presented as the mean with standard deviation bars. Poiseuille resistances are calculated with the morphometric data.

tion near these regions.[6,45] As Womersley number is larger in the adult, indicating the importance of transient flow, the velocity profile in the adult is characteristic of a Womersley profile, while the velocity profiles in the infant and child are more parabolic. As respiratory compliance increases with age (Table 2), the amount of pressure needed to drive flow in and out of the lung is higher (Fig. 3).

Airflow features may be distinguished between subject or age-specific phenomenon. Global non-dimensional parameters, Re_{mean} and Wo, should remain similar between subjects within the same age groups and breathing conditions. For example, as Re_{mean} is linearly proportional to both the characteristic length ($D_{trachea}$) and flow rate (Q_{mean}) a $\sim \pm 20\%$ variability in either the trachea diameter (Fig. 2) or mean flow rate would result in a $\sim \pm 20\%$ variability in Re_{mean}. These variances are not expected to significantly affect observed global flow characteristics: conducting airway velocity magnitudes (Fig. 5), pressure gradients (Fig. 4), and airway resistances (Fig. 10) are inversely correlated with age. However, flow characteristics that are linked to specific morphometric features (e.g., locations of recirculation near increases in airway cross-sectional area, Fig. 5, linkage of secondary flow strength with the main carina bifurcation angle, infant: Fig. 8, and correlation of reduced cross-sectional area and peak flow speeds within the main left bronchi, Fig. 5) are likely patient-specific and therefore not a phenomenon that would be observed in all healthy subject within a particular age group. Further investigations that model airflow for a large range of subjects would indeed help to distinguish, and correlate, patient-specific versus expected median observations.

Limited by the clinical thoracic CT images, it was impossible to capture the extra-thoracic airways with our models. Several previous works have focused on age differences in airflow with the extra-thoracic airways.[37,44] As highlighted in Xi *et al.*,[44] the nasopharynx is smaller and narrower in the juvenile models compared to the adult. These differences, coupled with the smaller airways, resulted in resistance values that were inversely correlated with age,[44] similar to the findings from this study. Combining respiratory-gated MRI and CFD, Persak *et al.*[37] found that the nasopharynx jet appears throughout the respiration cycle, with the oropharynx jet only appears during the second half of inspiration. These turbulent jets likely reach well into the trachea during inspiration,[5] and therefore may contribute to distal flow structures and resistances. In addition, as multiple images throughout the breathing cycle were not acquired and we do not have airway tissue material properties, it was not feasible to incorporate deformation into our frameworks. Experimental studies have shown that the trachea and main bronchi are more compliant in youth[8] and therefore dynamic simulations may be even more important than for adults.

In summary, by coupling image-based geometries with global respiratory mechanics, we provide better understanding of airflow and airway resistances within healthy infant, child, and adult conducting airways. Simulation results highlight similarities between locations of peak pressure drops, Reynolds numbers, and developed flow structures. In contrast, model predictions emphasized that peak flow speeds, pressure drops, and airway resistances are inversely correlated with age. We suggest that future studies focus on uncovering inter- and intra-subject variability within each age group, simulation of realistic breathing waveforms during various scenarios (e.g., exercising, crying, *etc.*), as well as calculating the fate of inhaled particulates.

ACKNOWLEDGMENTS

This work was supported by an ALA Senior Research Training Grant and a University of California Presidential Postdoctoral Fellowship (J. M. Oakes). The authors would like to thank Dr. Jeff Feinstein at Stanford University for providing the thoracic CT images and examining the resulting 3D airway geometries. In addition, we would like to thank Dr. Weiguang Yang for assisting with the CT images and Adam Updegrove for providing modeling expertise. The authors acknowledge the Information Technology Services, Research Computing at Northeastern University for providing high performance computing resources.

CONFLICT OF INTEREST

The authors have no conflict of interest related to the work presented in this manuscript.

REFERENCES

[1]Amirav, I., and M. T. Newhouse. Aerosol therapy in infants and toddlers: past, present and future. *Expert Rev. Respir. Med.* 2(5):597–605, 2008.

[2]Attinger, E., R. G. Monroe, and M. S. Segal. The mechanics of breathing in different body positions. I. In normal subjects. *J. Clin. Investig.*, 35(8):904–911, 1956.

[3]Burri, P. H. Structural aspects of postnatal lung development—Alveolar formation and growth. *Biol. Neonate*, 89(4):313–322, 2006.

[4]Carrigy, N. B., C. A. Ruzycki, L. Golshahi, and W. H. Finlay. Pediatric in vitro and in silico models of deposition via oral and nasal inhalation. *J. Aerosol Med. Pulm. Drug Deliv.*, 27(3):149–169, 2014.

[5]Choi, J., M. H. Tawhai, E. A. Hoffman, and C.-L. L. Lin. On intra- and intersubject variabilities of airflow in the human lungs. *Phys. Fluids*, 21(10):101901-1–17, 2009.

[6]Comer, J. K., C. Kleinstreuer, C. S. Kim. Flow structures and particle deposition patterns in double-bifurcation airway models. Part 2. Aerosol transport and deposition. *J. Fluid Mech.*, 435:55–80, 2001.

[7]Comerford, A., C. Förster, and W. A. Wall. Structured tree impedance outflow boundary conditions for 3D lung simulation. *J. Biomech. Eng.*, 132(8):081002:1–10, 2010.

[8]Croteau, J. R., and C. D. Cook. Volume-pressure and length-tension measurements in human tracheal and bronchial segments. *J. Appl. Physiol.*, 16:170–172, 1961.

[9]D'Angelo, E., E. Calderini, G. Torri, F. M. Robatto, D. Bono, and J. Milic-Emili. Respiratory mechanics in anesthetized paralyzed humans: effects of flow, volume, and time. *J. Appl. Physiol.*, 67(6):2556–2564, 1989.

[10]De Backer, J. W., W. G. Vos, C. D. Gorlé, P. Germonpré, B. Partoens, F. L. Wuyts, P. M. Parizel, and W. De Backer. Flow analyses in the lower airways: patient-specific model and boundary conditions. *Med. Eng. Phys.*, 30(7):872–879, 2008.

[11]Dubois, A. B., S. Y. Botelho, and J. H. Comroe. A new method for measuring airway resistance in man using a body plethysmograph: values in normal subjects and in patients with respiratory disease. *J. Clin. Investig.*, 35(3):327–335, 1956.

[12]Esmaily Moghadam, M., Y. Basikevs, and A. L. Marsden. A new preconditioning technique for implicitly coupled multidomain simulations with applications to hemodynamics. *Comput. Mech.*, 52:1141–1152, 2013.

[13]Esmaily Moghadam, M., Y. Bazilevs, T.-Y. Hsia, I. E. Vignon-Clementel, A. L. Marsden, and Alliance (MOCHA). A comparison of outlet boundary treatments for prevention of backflow divergence with relevance to blood flow simulations. *Comput. Mech.*, 48(3):277–291, 2011.

[14]Esmaily Moghadam, M., I. E. Vignon-Clementel, R. Figliola, and A. L. Marsden. A modular numerical method for implicit 0D/3D coupling in cardiovascular finite element simulations. *J. Comput. Phys.*, 244:63–79, 2013.

[15]Ginsberg, G., B. Foos, R. B. Dzubow, and M. Firestone. Options for incorporating children's inhaled dose into human health risk assessment. *Inhal. Toxicol.*, 22(8):627–647, 2010.

[16]Godfrey, S., P. L. Kamburoff, and J. R. Nairn. Spirometry, lung volumes and airway resistance in normal children aged 5 to 18 years. *Br. J. Dis. Chest*, 64(1):15–24, 1970.

[17]Hall, G. L., Z. Hantos, F. Petak, J. H. Wildhaber, K. Tiller, P. R. Burton, and P. D. Sly. Airway and respiratory tissue mechanics in normal infants. *Am. J. Respir. Crit. Care Med.*, 162:1397–1402, 2000.

[18]Hofmann, W. Mathematical model for the postnatal growth of the human lung. *Respir. Physiol.*, 49:115–129, 1982.

[19]Horsfield, K., G. Dart, D. E. Olson, G. F. Filley, and G. Cumming. Models of the human bronchial tree. *J. Appl. Physiol.*, 31(2):207–217, 1971.

[20]Horsfield, K., W. I. Gordon, W. Kemp, and S. Phillips. Growth of the bronchial tree in man. *Thorax*, 42:383–388, 1987.

[21]Kaczka, D. W., K. R. Lutchen, and Z. Hantos. Emergent behavior of regional heterogeneity in the lung and its effects on respiratory impedance. *J. Appl. Physiol.*, 110(5):1473–1481, 2011.

[22]Kleinstreuer C., and Z. Zhang. Airflow and particle transport in the human respiratory system. *Annu. Rev. Fluid Mech.*, 42(1):301–334, 2010.

[23]Koullapis, P. G., S. C. Kassinos, M. P. Bivolarova, and A. K. Melikov. Particle deposition in a realistic geometry of the human conducting airways: Effects of inlet velocity profile, inhalation flowrate and electrostatic charge. *J. Biomech.*, 49:2201–2212, 2016.

[24]Kruger, S. J., S. K. Nagle, M. J. Couch, Y. Ohno, M. Albert, and S. B. Fain. Functional imaging of the lungs with gas agents. *J. Magn. Reson. Imaging*, 43(2):295–315, 2016.

[25]Kuprat, A. P., S. Kabilan, J. P. Carson, R. A. Corley, and D. R. Einstein. A bidirectional coupling procedure applied to multiscale respiratory modeling. *J. Comput. Phys.*, 244:148–167, 2013.

[26]Lanteri C. J., and P. D. Sly. Changes in respiratory mechanics with age. *J. Appl. Physiol.*, 74(1):369–378, 1993.

[27]Ma B., and K. R. Lutchen. An anatomically based hybrid computational model of the human lung and its application to low frequency oscillatory mechanics. *Ann. Biomed. Eng.*, 34(11):1691–1704, 2006.

[28]Ma, B., and K. R. Lutchen. CFD simulation of aerosol deposition in an anatomically based human large-medium airway model. *Ann. Biomed. Eng.*, 37(2):271–85, 2009.
[29]Ménache, M. G., W. Hofmann, B. Ashgarian, and F. J. Miller. Airway geometry models of children's lungs for use in dosimetry modeling. *Inhal. Toxicol.*, 20(2):101–126, 2008.
[30]Miyawaki, S., S. Choi, E. A. Hoffman, and C. L. Lin. A 4DCT imaging-based breathing lung model with relative hysteresis. *J. Comput. Phys.*, 326:76–90, 2016.
[31]Morris, P. D., A. Narracott, H. von Tengg-Kobligk, D. A. Silva Soto, S. Hsiao, A. Lungu, P. Evans, N. W. Bressloff, P. V. Lawford, D. R. Hose, and J. P. Gunn. Computational fluid dynamics modelling in cardiovascular medicine. *Heart*, 102:18–28, 2016.
[32]Oakes, J. M., A. L. Marsden, C. Grandmont, C. Darquenne, and I. E. Vignon-Clementel. Distribution of aerosolized particles in healthy and emphysematous rat lungs: comparison between experimental and numerical studies. *J. Biomech.*, 48(6):1147–1157, 2015.
[33]Oakes, J. M., A. L. Marsden, C. Grandmont, S. C. Shadden, C. Darquenne, and I. E. Vignon-Clementel. Airflow and particle deposition simulations in health and emphysema: from in vivo to in silico animal experiments. *Ann. Biomed. Eng.*, 42(4):899–914, 2014.
[34]Oakes, J. M., M. Scadeng, E. C. Breen, A. L. Marsden, and C. Darquenne. Rat airway morhometry measured from in-situ MRI-based geometric models. *J. Appl. Physiol.*, 112:1921–1931, 2012.
[35]Oakes, J. M., S. C. Shadden, C. Grandmont, and I. E. Vignon-clementel. Aerosol transport throughout inspiration and expiration in the pulmonary airways. *Int. J. Numer. Method Biomed. Eng.*, e2847, 2017.
[36]Pedley, T. J., R. C. Schroter, and M. F. Sudlow. The prediction of pressure drop and variation of resistance within the human bronchial airways. *Respir. Physiol.*, 9(3):387–405, 1970.
[37]Persak, S. C., S. Sin, J. M. McDonough, R. Arens, and D. M. Wootton. Noninvasive estimation of pharyngeal airway resistance and compliance in children based on volume-gated dynamic MRI and computational fluid dynamics. *J. Appl. Physiol.*, 111(6):1819–1827, 2011.
[38]Phalen R. F., and M. J. Oldham. Methods for modeling particle deposition as a function of age. *Respir. Physiol.*, 128:119–130, 2001.
[39]Phalen, R. F., M. J. Oldham, C. B. Beaucage, T. Timothy Crocker, and J. D. Mortensen. Postnatal enlargement of human tracheobronchial airways and implications for particle deposition. *Anat. Rec.*, 212:368–380, 1985.
[40]Sá, R. C., M. V. Cronin, A. C. Henderson, S. Holverda, R. J. Theilmann, T. J. Arai, D. J. Dubowitz, S. R. Hopkins, R. B. Buxton, and G. K. Prisk. Vertical distribution of specific ventilation in normal supine humans measured by oxygen-enhanced proton MRI. *J. Appl. Physiol.*, 109(6):1950–1959, 2010.
[41]Tenenbaum-Katan, J., P. Hofemeier, and J. Sznitman. Computational models of inhalation therapy in early childhood: therapeutic aerosols in the developing acinus. *J. Aerosol Med. Pulm. Drug Deliv.*, 29:288–298, 2016.
[42]Tian, G., P. W. Longest, G. Su, R. L. Walenga, and M. Hindle. Development of a stochastic individual path (SIP) model for predicting the tracheobronchial deposition of pharmaceutical aerosols: effects of transient inhalation and sampling the airways. *J. Aerosol Sci.*, 42(11):781–799, 2011.
[43]Updegrove, A., N. M. Wilson, J. Merkow, H. Lan, A. L. Marsden, and S. C. Shadden. SimVascular: an open source pipeline for cardiovascular simulation. *Ann. Biomed. Eng.*, 45:525–541, 2017.
[44]Xi, J., A. Berlinski, Y. Zhou, B. Greenberg, and X. Ou. Breathing resistance and ultrafine particle deposition in nasal-laryngeal airways of a newborn, an infant, a child, and an adult. *Ann. Biomed. Eng.*, 40(12):2579–2595, 2012.
[45]Zhang, Z., and C. Kleinstreuer. Transient airflow structures and particle transport in a sequentially branching lung airway model. *Phys. Fluids,* 14(2):862–880, 2002.